Design considerations for λ ~ 3.0- to 3.5-μm-emitting quantum cascade lasers on metamorphic buffer layers

Ayushi Rajeev
Chris Sigler
Tom Earles
Yuri V. Flores
Luke J. Mawst
Dan Botez

Design considerations for $\lambda \sim 3.0$- to 3.5-µm-emitting quantum cascade lasers on metamorphic buffer layers

Ayushi Rajeev,[a] Chris Sigler,[a] Tom Earles,[b] Yuri V. Flores,[c] Luke J. Mawst,[a,*] and Dan Botez[a]

[a]University of Wisconsin–Madison, Department of Electrical and Computer Engineering, Madison, Wisconsin, United States
[b]Intraband LLC, Madison, Wisconsin, United States
[c]Massachusetts Institute of Technology, Research Laboratory of Electronics, Cambridge, Massachusetts, United States

Abstract. Quantum cascade lasers (QCLs) that employ metamorphic buffer layers as substrates of variable lattice constant have been designed for emission in the 3.0- to 3.5-µm wavelength range. Theoretical analysis of the active-region (AR) energy band structure, while using an 8-band k•p model, reveals that one can achieve both effective carrier-leakage suppression as well as fast carrier extraction in QCL structures of relatively low strain. Significantly lower indium-content quantum wells (QWs) can be employed for the AR compared to QWs employed for conventional short-wavelength QCL structures grown on InP, which, in turn, is expected to eliminate carrier leakage to indirect-gap valleys (X, L). An analysis of thermo-optical characteristics for the complete device design indicates that high-Al-content AlInAs cladding layers are more effective for both optical confinement and thermal dissipation than InGaP cladding layers. An electroluminescence-spectrum full-width half-maximum linewidth of 54.6 meV is estimated from interface roughness scattering and, by considering both inelastic and elastic scattering, the threshold-current density for 3.39-µm-emitting, 3-mm-long back-facet-coated QCLs is projected to be 1.40 kA/cm². © *The Authors. Published by SPIE under a Creative Commons Attribution 3.0 Unported License. Distribution or reproduction of this work in whole or in part requires full attribution of the original publication, including its DOI.* [DOI: 10.1117/1.OE.57.1.011017]

Keywords: quantum cascade laser; metamorphic buffer layer; semiconductor laser; metalorganic chemical vapor deposition.

Paper 170925SS received Jun. 15, 2017; accepted for publication Aug. 30, 2017; published online Sep. 27, 2017.

1 Introduction

High-power lasers operating in the mid-infrared (IR) spectral region with emission in the 3.0- to 3.5-µm wavelength range have garnered interest due to applications such as advanced remote sensing and ranging. High-performance, low threshold-current density, interband-transition lasers have been reported within the 3.0- to 3.5-µm wavelength range by employing either type-I quantum wells (QWs)[1–3] or type-II QWs (i.e., interband cascade lasers).[4–6] However, such devices are highly temperature sensitive due to hole leakage (in the case of type-I QW devices) as well as Auger recombination and/or Auger-assisted carrier leakage.[1–8] As a result, such devices exhibit low threshold-current characteristic temperature coefficients, T_0, and low slope-efficiency characteristic temperature coefficients, T_1.[1–6] Since the maximum CW power, P_{max}, is a strong function[9–11] of T_0 and especially T_1 values, this explains why the P_{max} values have been relatively low (<500 mW) from both type-I and type-II QW lasers operating in this wavelength range.

Quantum cascade lasers (QCLs), being intersubband (ISB)-transition devices, do not suffer from Auger recombination, thus relatively high T_0 values can be obtained[11] and have achieved a wide range of emission wavelengths using a single-material system for designing and fabricating devices. However, when using conventional substrates, such as InP and GaAs, the materials constituting the superlattice (SL) core region of the QCL are constrained by strain-induced critical-thickness limitations. It is well known that the degree of strain relaxation induced increases as one approaches the critical thickness of the individual (compressive-strained)

QW and (tensile-strained) barrier layers constituting the SL, thus leading to subsequent device failure. Strain relaxation can also develop if the average strain of the SL core region becomes too large. However, the actual strain limits that can be tolerated without relaxation are impacted by kinetic factors, which, in turn, depend on the growth temperature and growth rate.

The imposed strain limitations are in direct conflict with one of the foremost requirements for QCLs in the 3.0- to 3.5-µm wavelength regime, which is to have large conduction-band (CB) offsets between wells and barriers in order to accommodate the high transition energies. Even if strain relaxation is not present, high strain affects the interface morphology[12,13] in the active regions (ARs) of the stages of the QCL core region, which, in turn, is expected to impact the device performance. InP-based 3.56-µm-emitting QCLs[14] have demonstrated high CW output power (0.5 W), although such devices utilize InGaAs/AlInAs-SL ARs of highly strained ($\Delta a/a \sim 2\%$) QWs and barriers. While relatively high T_0 values (152 to 166 K) were obtained, the T_1 value was moderately high (∼190 K) only for 3.56-µm-emitting devices, as it dropped to ∼116 K for 3.39-µm-emitting devices, most likely due to the onset of leakage to satellite valleys.[15] Similarly, 3.3-µm-emitting devices[16] have displayed low T_1 values (∼71 K), over the 250- to 300-K temperature range, indicating strong carrier leakage to satellite valleys. The T_0 values were also found to be low (100 K) above an operating temperature of 250 K, due to carrier leakage and possibly strong backfilling, considering the relatively high injector-doping level. Even higher strain ($\Delta a/a \sim 3\%$) barriers have been used to enable the emission wavelength to be as short as 3.0 µm,[17] although very low T_0 and T_1 values limited the CW output power to quite low

values ($\sim$2.5 mW). Such poor performance was most likely due to strong carrier leakage to satellite valleys (L, X) for $\sim$3.05-μm-emitting devices grown on InP.[18]

We have previously proposed the use of metamorphic buffer layers (MBLs) as the means to achieve high-performance low-strain QCLs at 3.0- to 3.5-μm emission wavelengths.[19,20] These "virtual substrates" under consideration were grown on (001) GaAs substrates by hydride vapor phase epitaxy.[21] They consisted of nine $In_xGa_{1-x}As$ layers with linear grading of the In content in each of the nine $\sim$1.0-μm-thick steps. The final layer was a constant-composition cap layer which is typically $\sim$15-μm thick to allow for surface preparation in order to perform the regrowth of strained layers atop with high fidelity.[20] The MBL cap is found to be nearly fully relaxed ($>$95%), owing to its thickness, and exhibits tilt with respect to the substrate, which is a function of composition and thickness.[13,21] The MBL enables trapping of misfit dislocations at the composition steps while forcing the threading dislocations to glide to the edges of the sample, thus giving us a virtual substrate with a threading-dislocation density of the order of $\sim$10^5 cm^{-2}. However, the induced strain relaxation in the MBL results in a cross-hatched surface morphology which is detrimental to QCL-device performance. The use of chemical–mechanical planarization (CMP) with appropriate applied pressure on the MBL cap was found to reduce the cross-hatching height by more than 20 times.[22] A single stage of the QCL structure grown atop an MBL, which had undergone the CMP treatment, did result in electroluminescence (EL) emission near 3.6-μm wavelength from mesa devices tested at 80 K.[21] However, indium enrichment was observed in the MBL cap layer when heated to high-regrowth temperatures. An additional wet-chemical etching step introduced after the CMP resolved this issue and provided an epi-appropriate surface for regrowth of strained SL layers.[20] Ten stages of the QCL structure of the AR design for 3.4-μm emission target wavelength were grown with high fidelity on an MBL using the aforementioned optimized surface treatment, as confirmed by x-ray diffraction and transmission electron microscopy.[20] To enable growth of the complete laser design, several challenges remain such as the choice of cladding material and optical-waveguide design, which are being addressed in this study. Moreover, the structural, thermal, and optical characteristics of the ternary cladding material, with specific compositions that are lattice-matched to the MBL, have not been previously reported.

A direct consequence of using MBLs is the expansion of the design space for QCLs emitting at mid-IR wavelengths by having an application-oriented custom-grown substrate. Here, we perform a comprehensive design optimization of a particular AR design based on an MBL employing an $In_{0.22}Ga_{0.78}As$ cap layer. A thermo-optical analysis for the complete laser design indicates that the use of $In_xAl_{1-x}As$ cladding layers allows for both good optical confinement and adequate heat transport.

2 Quantum Cascade Laser Design

2.1 Quantum Cascade Laser Active-Region Design

To analyze the design of the QCL ARs grown on MBLs, the energy-band structure, electronic wavefunctions, and electron energy-state lifetimes have been calculated using an 8-band k•p code, as previously reported.[19] Conventional QCL structures utilize fixed compositions for the wells and barriers with variations only in the thickness of each layer type. For such QCLs, it has been found[11] that for 3.76-μm-emitting devices[23] one can achieve both efficient carrier-leakage suppression and fast, miniband-like carrier extraction when using, for lower-laser-level depopulation, the single-phonon-resonance (SPR) AR structure in conjunction with resonant-tunneling extraction from the lower laser level.[24] We have achieved the same type of AR design (i.e., SPR + miniband extraction) for our short-wavelength ($\lambda = 3.0$ to 3.5 μm) QCL structures grown on MBLs. More specifically, an SPR + miniband extraction AR design was reached given a lattice constant of 0.574 nm for the virtual substrate (i.e., the cap layer of the MBL) so as to provide a relatively low-strain QCL structure for emission in the 3.0- to 3.5-μm wavelength range. Such a design, based on an MBL cap composition of $In_{0.22}Ga_{0.78}As$, with a 10-stage core region consisting of AlAs barriers and $In_{0.45}Ga_{0.55}As$ wells, and designed to emit at 3.39 μm has been grown by using metalorganic chemical vapor deposition (MOCVD) of high crystalline quality.[20] The layers thicknesses (expressed in Å) within one stage of the QCL core region are as follows: **25**/16/**24**/17/**21**/18/**20**/21/**19**/21/**18**/18/**17**/28/**12**/13/**39**/10/**33**/16. The bold-faced layers are the wells and the other layers are barriers, with the doped layers (n-type, 2×10^{17} cm^{-3}) indicated by italics. Figure 1 shows the CB diagram and relevant electronic wavefunctions for this design at the indicated applied electric field.

2.2 Complete Quantum Cascade Laser Structure: Thermo-Optical Analysis

The AR modeling is followed by the 1-D optical analysis of the complete laser structure shown in Fig. 2. This makes use of a wave-transfer matrix method for TM-polarized light. Using the refractive-index profile of this structure (Table 1), the wave-transfer matrix method[25] is employed to analyze the optical confinement and mode profiles obtained. We consider two different cladding materials, $In_xAl_{1-x}As$ and $In_xGa_{1-x}P$, since both materials can be lattice matched to the MBL and have refractive indices lower than the average refractive index of the SL core region.
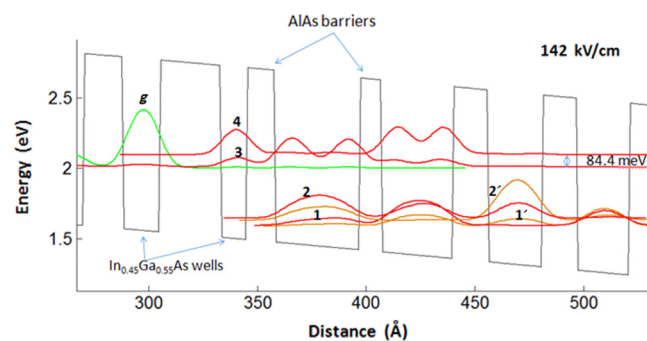
Fig. 1 CB diagram and modulus squared of the most relevant wavefunctions shown at the operating electric field at threshold (142 kV/cm) for a 3.39-μm-emitting, SPR + miniband-extraction QCL design grown on an $In_{0.22}Ga_{0.78}As$ MBL cap layer. The primed numbers identify wavefunctions from the extractor region that penetrate into the AR.
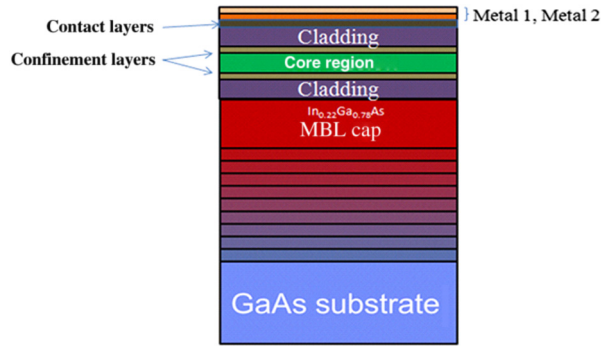
Fig. 2 Complete laser structure showing the upper and lower optical-confinement layers and the cladding layers.

As the MBL cap is ~ 10-μm thick and nearly fully relaxed, for all simulations, the constant composition in the cap (i.e., $In_{0.22}Ga_{0.78}As$) is treated as a substrate. The upper and lower-cladding layers are grown lattice matched to the MBL cap and consist of either $In_{0.21}Al_{0.79}As$ or $In_{0.69}Ga_{0.31}P$. The upper and lower optical-confinement layers are $In_{0.22}Ga_{0.78}As$. The QCL core region comprises 30-stages, with the layer thicknesses and doping levels for a stage described above. The last semiconductor layer grown is a highly n-type-doped contact/plasmon layer, which is $In_{0.21}Al_{0.79}As$ or $In_{0.69}Ga_{0.31}P$. An additional thin, highly doped $In_{0.22}Ga_{0.78}As$ contact layer could be grown on top to provide a low-resistance ohmic contact, although this is not included in the model for simplicity. This is followed by Ti/Au metal contact layers.

The Drude model is employed to determine the refractive indices of each of these layers for an emission wavelength of 3.4 μm. Specifically, for the core region, the refractive index is obtained by averaging over 30 stages of alternating well and barrier layers and also taking into account the injector layers that are intentionally doped. Refractive indices for the metal layers are obtained from Refs. [26] and [27].

The thermal analysis for the structure is conducted using the heat transfer module of the COMSOL Multiphysics software package. Steady-state equations are employed for

Table 1 List of material parameters employed for thermo-optical analysis of the complete laser structure. Only the real part of the refractive indices are noted here, although imaginary parts will be used for the calculation of losses as discussed below.

Layer name	Composition/doping	Refractive index (n)
MBL cap	$In_{0.22}Ga_{0.78}As/2 \times 10^{17}$ cm^{-3}	3.347
Lower/upper cladding	$In_{0.21}Al_{0.79}As/2 \times 10^{16}$ cm^{-3}	2.993
	$In_{0.69}Ga_{0.31}P/2 \times 10^{16}$ cm^{-3}	3.075
Lower/upper confinement	$In_{0.22}Ga_{0.78}As/4 \times 10^{16}$ cm^{-3}	3.346
Core region	Section 2.1	3.158
Contact/plasmon layer	$In_{0.21}Al_{0.79}As/5 \times 10^{18}$ cm^{-3}	2.918
	$In_{0.69}Ga_{0.31}P/5 \times 10^{18}$ cm^{-3}	2.967

Table 2 List of the material parameters employed for thermal analysis of the complete laser structure. The room-temperature estimated thermal conductivity is provided where the temperature dependence is not well-known.

Layer name	Composition	Thermal conductivity (W/m · K)
MBL cap[29,30]	$In_{0.22}Ga_{0.78}As$	6.694
Lower/upper cladding[29,31]	$In_{0.21}Al_{0.79}As$	8.621
	$In_{0.69}Ga_{0.31}P$	5.946
Lower/upper confinement[29,31]	$In_{0.22}Ga_{0.78}As$	6.694
Core region[32]	Section 2.1	$k_{\parallel} = 5.3 - 3.9 \times 10^{-3} T$ $+ 5.3 \times 10^{-7} T^2$ $k_{\vert} = 2.3$
Plasmon/contact layer[29,31]	$In_{0.21}Al_{0.79}As$	8.621
	$In_{0.69}Ga_{0.31}P$	5.946
Gold[32]	—	$337 - 660 \times 10^{-4} T$
Titanium[32]	—	$31.46 - 4.338 \times 10^{-2} T$ $+ 4 \times 10^{-5} T^2$
Copper[32]	—	$349 + 14710 T^{-1}$
Diamond[33]	—	1800
Indium solder[32]	—	$1.9 - 6.96 \times 10^{-2} T$ $+ 9.86 \times 10^{-5} T^2$

analyzing the thermal dissipation under CW operation of the QCL. The QCL is considered to be processed to form ridge waveguides 10-μm wide. A two-step gold electroplating process will then be employed to fill in the trenches and obtain a planar top surface for mounting.[28] The chip will be mounted in epi-down fashion using 4-μm-thick indium solder on a 300-μm-thick diamond submount already bonded to a copper heatsink, which will be 1.5-mm thick and 3-cm wide. The boundary conditions for the packaged chip are set as room temperature for the bottom of the heatsink, with the other boundaries being adiabatic.

The thermal conductivities are listed for all the materials involved in fabricating and packaging this laser, providing the temperature dependences where known (Table 2). The challenge, as stated earlier, is to estimate the appropriate value of thermal conductivities for the two cladding-layer options for this QCL design: $In_{0.21}Al_{0.79}As$ and $In_{0.69}Ga_{0.31}P$. The dependence of thermal resistivity of a ternary alloy on the binary-compound resistivities is as follows:[29]

$$T_{A_x B_{1-x} C}(x) = x B_{AC} + (1-x) B_{BC} + C_{A-B} x(1-x), \quad (1)$$

where C_{A-B} is the bowing parameter owing to the lattice disorder originating from the random distribution of A and B atoms on the interchangeable sublattice sites.

C_{In-Ga} has been calculated to be 72 W^{-1} deg cm at room temperature from fitting the thermal resistivity data of InAs-GaAs alloys and is assumed to be the same for InP-GaP alloys. This bowing parameter results in thermal resistivities that are in good agreement with those experimentally determined for $In_x Ga_{1-x}P$ layers of different x concentration.[34,35]

The disorder alloy-bowing parameter for InAlAs is estimated to be 60 W^{-1} deg cm.[31] These are yet to be confirmed experimentally. The thermal resistivities for the binary alloys under consideration, namely InAs, AlAs, InP and GaP, have all been well characterized.[29]

The anisotropic thermal conductivity for the core region is assumed to be close to that obtained for a conventional 4.6-μm-emitting QCL.[32] This is expected to suffice for the purpose of comparing the effectiveness of using InAlAs versus InGaP as cladding-layer materials.

3 Results and Discussion

Key parameters used in determining the device performance, for the 3.39-μm-emitting AR design shown in Fig. 1, are listed in Table 3. For this optimized AR design, resonant-tunneling extraction (to the next injector region) occurs from both the lower laser level (state 2) and the state below it (state 1), which constitutes miniband-like extraction.[11] In turn, as evident from Table 3, the lower-laser-level global lifetime[36] $\tau_{22'g}$ (0.195 ps) is basically half the value of that for the SPR-only 3.56-μm-emitting QCLs grown on InP[14] (i.e., 0.397 ps). As a result, the room-temperature slope efficiency is expected to be significantly higher, due to both higher laser-transition differential efficiency,[11,24] and, as discussed below, less carrier leakage, just as in the case of SPR + miniband extraction, 3.76-μm-emitting QCLs[23] versus SPR-only, 3.56-μm-emitting QCLs.[14] The upper-laser-level global lifetime τ_{3g} requires a delicate balance of maximizing its value (often easily obtained by having extended wavefunctions throughout the AR and beyond) with the opposing need for a highly vertical laser transition. Keeping the ratio of

Table 3 Key parameters for SPR + miniband extraction QCL-structure designs grown on an MBL: the operating field at threshold; the energy difference between the upper laser level, state 3, and the next higher AR energy state, state 4, E_{43}; the energy level separation between the lower laser states (states 2 and 2′) and the ground state of the next-stage injector, Δ_{inj}; the dipole matrix element between the upper laser level and lower laser level, z_{32g}; the lifetime of transitions between state 4 and state 3, τ_{43}, the global lifetimes for the upper and lower laser states, τ_{3g} and $\tau_{22'g}$; the average strain per stage; and the strain of well and barrier layers. For comparison, we also show the same parameters for SPR-only QCLs on InP.[14]

3.39-μm design on In$_{0.22}$Ga$_{0.78}$As MBL	3.56-μm design on InP[14]
Operating field = 142 kV/cm	194 kV/cm
$E_{43} = 84.4$ meV	$E_{43} = 65.1$ meV
$\Delta_{inj} = 226.41$ meV	$\Delta_{inj} = 391.2$ meV
$z_{32g} = 11.09$ Å	$z_{32g} = 10.36$ Å
$\tau_{3g} = 1.156$ ps	$\tau_{3g} = 1.904$ ps
$\tau_{32g} = 1.81$ ps	$\tau_{32g} = 3.521$ ps
$\tau_{22'g} = 0.195$ ps	$\tau_{2g} = 0.397$ ps
$\tau_{43} = 0.51$ ps	$\tau_{43} = 0.548$ ps
Average strain per stage = −0.00284	+0.00148
Strain per barrier, well pair = +1.42%, −1.61%	+2.32%, −1.85%

upper laser levels' lifetimes and lower laser levels' lifetimes relatively large enables effective population inversion.

In structures with resonant extraction from the lower laser level both that level (state 2 in this case) and the extractor level (state 2′) are considered for the lasing transition.[24] Thus, the dipole matrix element is a global one, z_{32g}, taking into account transitions from both (energy) levels 3 to 2 and from levels 3 to 2′, and signifies the degree of overlap between the corresponding wavefunctions. τ_{32g}, the global lifetime for the laser transition, needs to be maximized such that the global, effective upper-level lifetime[36] converges to τ_{3g} as the lifetime ratio $\tau_{22'g}/\tau_{32g}$ approaches zero.

The figure of merit (FOM) using these critical parameters, for a first-order approximation of the threshold-current density, J_{th}, is as follows:[37]

$$\text{FOM} = |z_{32g}|^2 \times \left\{ \tau_{3g} \left(1 - \frac{\tau_{22'g}}{\tau_{32g}} \right) \right\}, \tag{2}$$

and since the backfilling current is negligible in both structures, due to very large values for the energy difference (at threshold) between the lower laser level, state 2, and the ground level, state g, in the next injector Δ_{inj} (Table 3), one obtains

$$J_{th} \propto \frac{1}{\text{FOM}}. \tag{3}$$

The illustrated QCL design has an FOM value of 127.9 Å^{2}ps compared to the calculated value of 181.3 Å^{2}ps for the 3.56-μm QCL grown on InP.[14] However, the FOM values do not take into account the carrier leakage from the upper laser level, which, as discussed below, is significantly lower for our 3.39-μm QCL design on MBL than for the 3.56-μm-emitting QCL design on InP. Thus, the actual difference between the achievable J_{th} values for the two devices will definitely be lower than indicated by the calculated FOM values.

The relatively large value for the energy difference between the upper laser level, state 3, and the next higher AR energy level, state 4, E_{43}, of the 3.39-μm QCL on MBL (i.e., 84.4 meV) will result in negligible carrier leakage through thermal excitation from state 3 to state 4 and consequent relaxation to the lower AR energy states (i.e., to 1, 1′, 2, and 2′).[38] This will happen because the E_{43} value strongly impacts the scattering rate from state 3 to state 4 ($1/\tau_{34}$) and, in turn, the leakage-current density J_{leak}.[38] The former is estimated as follows, given an electronic temperature T_{e3} in state 3:[39,40]

$$\frac{1}{\tau_{34}} \approx \frac{1}{\tau_{43}} \exp\left(-\frac{E_{43}}{kT_{e3}} \right). \tag{4}$$

To reduce the scattering rate into the upper AR energy states (i.e., $1/\tau_{34}$), we designed QCLs with large E_{43} and τ_{43} values. The resulting design characteristics, related to the device performance, are reduced temperature sensitivities for the threshold-current density, J_{th}, and the slope efficiency, η, (i.e., higher T_0 and T_1 values) and subsequently increased maximum CW power, P_{max}, and maximum CW wallplug efficiency, $\eta_{wp,max}$, due to higher values for T_0 and especially higher values for T_1.[10,11,36] From Table 3, one can see that

while the τ_{43} values are similar for the two compared devices, the E_{43} value is higher for 3.39-μm QCLs on MBL than for 3.56-μm QCLs on InP (i.e., 84.4 meV versus 65.1 meV). This is consistent with the fact that the E_{43} value generally decreases with increasing field strength; thus, given that the 3.56-μm QCLs on InP has a significantly higher field strength than our 3.39-μm device on MBL (i.e., 194 versus 142 kV/cm), the higher E_{43} value for the device grown on MBL is justified. Since, as seen from Eq. (4), the scattering rate to the upper AR states is an exponential function of $-E_{43}$, the carrier leakage will be significantly lower for 3.39-μm QCLs on MBL than for 3.56-μm QCLs on InP. We note that for these 3.4-μm-emitting QCLs on MBL we have been able to achieve both carrier-leakage suppression as well as miniband-like extraction without the need for deep QWs in the AR[24,41] or tapered barrier heights in the AR.[11,24,36] In addition, carrier leakage to satellite valleys (L, X) is also substantially reduced owing to the lower In percentage in QWs (i.e., 45%) for this QCL on MBL when compared to conventional QCLs grown on InP substrates for the wavelength range being studied (e.g., 80% for 3.56-μm-emitting QCLs[14] and 72% for 3.3-μm-emitting QCLs[16]). As pointed out above in Sec. 1, with increasing strain, which means with increasing In content in the QWs, such leakage becomes a significant portion of the total room-temperature J_{th} value for devices grown on InP, unlike devices designed for emission in the 3.5- to 4.0-μm range.[15,42,43]

Large Δ_{inj} values, like the ones in Table 3, ensure that the backfilling-current density due to thermal excitation from the ground state in the injector region of a stage to the lower laser level in the AR of the previous stage is minimized. However, a trade-off exists here as too large a value for Δ_{inj} will result in undesirably high voltages. Note that the QCL design on MBL presented in Table 3 has a significantly lower Δ_{inj} value compared to that for the QCL design on InP. This will result in a reduction in operating voltage, yet the Δ_{inj} value is large enough to minimize carrier backfilling, as further discussed below.

Other important characteristics for this design are a low average strain per stage (here: net compressive) and a fairly vertical lasing transition from state 3 to state 2, as seen in the AR band diagram (Fig. 1). Moreover, it is important to note that these specific compositions would result in +3.54% strain in the wells and +0.558% strain in the barriers if the SL would have been grown on InP. That is, the QW strain value would be extremely large in addition to the fact that both wells and barriers would be tensilely strained, thus ineffective in achieving strain compensation in the AR. We also note that the degree of strain balancing is much better for the device grown on MBL than for the device grown on InP.

As shown in Table 4, the limiting strain-thickness product for a barrier in the AR for this design is only 30% of that for the 3.0-μm-emitting QCL on InP[17] and 56% of that for the 3.56-μm-emitting QCL on InP.[14] Interestingly, the MBL-based design also compensates extremely well the limiting strain-thickness product for the wells and barriers in the injector region. The significantly lower strain values for the MBL-based QCL designs, compared to those for conventional short-wavelength QCLs, alleviate the issues of strain relaxation and may ultimately lead to improved device reliability for 3.0- to 4.0-μm-emitting QCLs.

Table 4 Strain × thickness products in units of Angstroms for the QCL design on MBL, compared with QCLs on InP substrate.

		QCL on MBL (3.39 μm)	QCL on InP[17] (3.0 μm)	QCL on InP[14] (3.56 μm)
Injector region	Well	−0.403	−0.445	−0.444
	Barrier	0.397	0.531	0.786
AR	Well	−0.629	−0.570	−0.612
	Barrier	0.184	0.614	0.324

Optical-mode confinement analysis is performed by combining the designed core region with cladding and optical-confinement layers forming the complete laser structure.

The refractive-index steps between the $In_{0.21}Al_{0.79}As$ cladding layers and the core region are higher than when using $In_{0.69}Ga_{0.31}P$ cladding layers. Straightaway, this gives superior optical-mode confinement to the core region when using InAlAs cladding layers. The threshold-current density is calculated as follows:[11,24]

$$J_{th} = \frac{\alpha_m + \alpha_{w,\text{eff}}}{\eta_{\text{inj,tot}}\Gamma g} = \frac{\alpha_m + \alpha_{w,\text{sim}} + \alpha_{\text{isb,bf}}}{\eta_{\text{inj}}\eta_p\Gamma g}, \quad (5)$$

where α_m is the mirror loss, $\alpha_{w,\text{sim}}$ is the simulated loss that includes free-carrier absorption losses and radiation leakage loss to the substrate owing to the antiguided nature of the transverse waveguide in the structure, $\alpha_{\text{isb,bf}}$ is the sum of ISB absorption losses in the injector regions and the equivalent loss corresponding to backfilling, $\eta_{\text{inj,tot}}$ is the total injection efficiency, η_{inj} is the tunneling-injection efficiency into the upper laser level, η_p is the pumping efficiency which reflects the degree of carrier leakage (i.e., $\eta_p = 1 - J_{\text{leak}}/J_{th}$), Γ is the (transverse) optical-mode confinement factor to the core region, and g is the differential gain in the case of unity tunneling-injection efficiency and no carrier leakage.[11]

The loss term $\alpha_{\text{isb,bf}}$ can be considered to be negligible for these devices for the following reasons: (1) the ISB absorption, a measure of optical losses in the injector regions due to absorption between minibands, drops fast with emission wavelength (i.e., from $\sim$2.3 cm^{-1} at $\lambda = 8.8$ μm[24] to $\sim$0.5 cm^{-1} at $\lambda = 4.6$ μm[44]) since with increased CB offset the injector-region minibands are further apart energywise, thus, since for our case the CB offset is significantly larger than for 4.6-μm-emitting devices, the ISB absorption will become negligible; (2) the backfilling-current density, J_{bf}, will be negligible since the Δ_{inj} value is rather large (i.e., 226 meV) compared to values in the 120- to 150-meV range for 4.6-μm-emitting QCLs and given that $J_{bf} \propto \exp(-\Delta_{inj}/kT_{eg})$.[11]

The device cavity length is taken to be 3 mm, and the reflectivities for the high-reflectivity (HR)-coated back facet and the uncoated front facet are taken to be 97% and 27%, respectively. The value for differential gain g is calculated using the expression for gain cross-section g_c[37] divided by Γ and multiplied by $\tau_{\text{up},g}$, the global, effective upper-state lifetime[36,37]

$$g = \tau_{\text{up},g} \times \frac{4\pi e}{\varepsilon_0 n_{\text{refr}} \lambda} \frac{z_{32g}^2}{2\gamma_{32} L_p}, \tag{6}$$

where $\tau_{\text{up},g}$, accounting for population inversion and electrical pumping, is given as

$$\tau_{\text{up},g} = \tau_{3g}\left(1 - \frac{\tau_{22'g}}{\tau_{32_g}}\right), \tag{7}$$

$2\gamma_{32}$ is the full-width half maximum (FWHM) broadening of the transition, as obtained from EL measurements, L_p is the thickness of one stage, λ is the emission wavelength of the QCL, and n_{refr} is the average refractive index for the AR as per the design.

We use the 4.6-μm-emitting QCL by Lyakh et al.[45] as the standard device for comparison to our design, as far as the value of the $\eta_{\text{inj,tot}}\, g$ product, due to the similarity in crystal-growth method employed (i.e., MOCVD) for the core region.

First of all, for $\eta_{\text{inj,tot}}$, we consider a typical η_{inj} value of 0.97, and for η_p we take 0.85, since those devices had strong carrier leakage as evidenced by a low T_1 value of 140 K[46] which we have shown[38] to correspond to $\eta_p \approx 0.85$ for conventional 4.6- to 4.7-μm-emitting QCLs. Then $\eta_{\text{inj,tot}} = 0.82$. Further confirmation that 0.82 is a good estimate for the $\eta_{\text{inj,tot}}$ value is the relatively large discrepancy found by Maulini et al.[44] between calculated and experimental wall-plug efficiency values [i.e., a factor of 0.77 that corresponds to ~ 0.80 for $\eta_{\text{inj,tot}}$ when taking into account the small deviation from linearity ($\sim 4\%$) of the pulsed $L - I$ curve at drives corresponding to the maximum wallplug efficiency].

As for g, one can use the parameters provided in Ref. 45 with the exception of the $\tau_{\text{up},g}$ value for which the lifetimes provided in Ref. 45 take into account only longitudinal optical phonon scattering; that is, only inelastic scattering. Fortunately, the same structure was studied in Ref. 46, and good agreement with experiment was found when $\tau_{4g,\text{inelastic}} = 1.1$ ps and $\tau_{4g,\text{elastic}} = 1.5$ ps. [The elastic part is primarily due to interface-roughness (IFR) scattering.] Then, the total global upper-state lifetime $\tau_{4g,\text{tot}}$ is 0.635 ps, that is, 1.73 times lower that $\tau_{4g,\text{inelastic}}$.

Thus, the value for the $\eta_{\text{inj,tot}}\, g$ product calculated without considering elastic scattering: 14.7 cm/kA, reduces to a value of 6.97 cm/kA (when elastic scattering is considered). We note that this estimated value is in excellent agreement with the experimental value of 6.8 cm/kA;[45] thus, it gives us confidence that applying the same procedure will provide a reasonably accurate value for the $\eta_{\text{inj,tot}}\, g$ product, as needed in order to estimate the potential J_{th} values for 3.39-μm-emitting QCLs on MBLs.

The room-temperature J_{th} value for the 4.6-μm-emitting QCL was 1.5 kA/cm^2 for a 40-stage core-region device.[45] We scaled it to 1.73 kA/cm^2 for direct comparison to 30-stage core-region devices. Moreover, when considering a 3-mm-long cavity with one HR-coated back facet, the J_{th} value becomes 1.28 kA/cm^2 (see Table 5). Having obtained good agreement between calculated J_{th} values and experimental results, the same estimation procedure is applied to the 3.39-μm-emitting QCL-on-MBL design.

An EL spectral linewidth, $2\gamma_{32g}$, of ~ 50 meV is expected, that is, a similar value as for ~ 3.76-μm-emitting QCLs of similar QW and well strain (i.e., $\sim \pm 1.5\%$) and same

Table 5 Calculated IFR ISB scattering rate and times for selected states of the 3.39-μm-emitting QCL on MBL design. Involved levels are labeled as in Fig. 1.

Involved levels	Scattering rate (ps^{-1})	Scattering time (ps)
3–2	0.672	1.486
3–2′	0.316	3.156
3–1	0.28	3.518
3–1′	0.106	9.405

lower-level depopulation scheme (i.e., SPR + miniband extraction).[23] As a matter of fact, the EL linewidth in mid-IR QCLs is primarily due to IFR scattering,[47] and we calculate a value of $2\gamma_{32g} \sim 54.6$ meV for the 3.39-μm-emitting QCL on MBL design. The calculated EL spectrum is shown in Fig. 3. The EL spectrum in this design will be primarily due to radiative transitions from level 3 into levels 2 and 2′ (Fig. 1). Furthermore, because of the lower optical dipole matrix element for the 3 to 2′ radiative transition compared to the 3 to 2 transition (4.5 versus 10.1 Å), the intensity of the 3 to 2′ EL component is reduced by a factor of ~ 5.1. The FWHM values of the individual EL spectra correspond to the IFR-induced inhomogeneous broadening values between the involved levels and are calculated as in Refs. 48 and 49

$$\gamma_{3,(2,2')}^{\text{IFR}} = \frac{\pi m_c}{\hbar^2} \Delta^2 \Lambda^2 \sum_i \Delta_{\text{CB}}^2 [\varphi_3^2(z_i) - \varphi_{(2,2')}^2(z_i)]^2, \tag{8}$$

where $m_c = 0.0472 m_0$ is the CB effective mass in the In$_{0.45}$Ga$_{0.55}$As QW material, $\Delta = 0.14$ nm is the in-depth roughness height and $\Lambda = 6$ nm is the in-plane roughness correlation length, $\Delta_{\text{CB}} = 1.2$ eV is the gamma-valley CB offset for the In$_{0.45}$Ga$_{0.55}$As/AlAs heterointerface, and $\varphi_{3,(2,2')}(z_i)$ are the wavefunction amplitudes of the involved levels at the i'th interface. It is important to note that minimal adjustment of the roughness parameters (Δ, Λ) was used with respect to values reported in the literature, as for example in
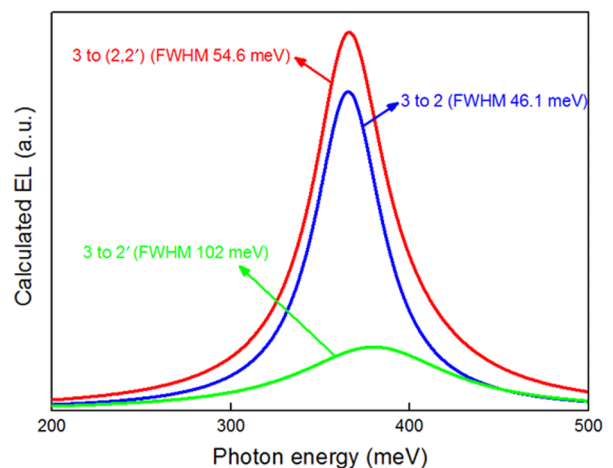
Fig. 3. Calculated EL spectrum for the 3.39-μm-emitting QCL on MBL design (Fig. 1). Inhomogeneous broadening due to IFR scattering has been considered for calculations.

Ref. 50. Specifically, we use $\Delta = 0.14$ nm and $\Lambda = 6$ nm, whereas $\Delta = 0.15$ nm and $\Lambda = 6$ nm were used in Ref. 50. In our consideration, such fluctuations in the roughness parameters are expected in the analysis of samples from different labs/growth sources. Altogether, we find excellent agreement between calculated (54.6 meV) and expected ($\sim$50 meV) $2\gamma_{32g}$ values.

Table 5 summarizes calculated scattering times for IFR-induced ISB scattering between selected states of the 3.39-μm-emitting QCL on MBL design. These values are calculated as in Ref. 50

$$\frac{1}{\tau_{m,n}^{IFR}} = \frac{\pi m_c}{\hbar^3} \Delta^2 \Lambda^2 \sum_i \Delta_{CB}^2 \varphi_m^2(z_i)\varphi_n^2(z_i) \exp\left(\frac{-\Lambda^2 m_c E_{mn}}{2\hbar^2}\right),$$

(9)

with $m = 3$ and $n = 2, 2', 1, 1'$ as in Fig. 1. E_{mn} is the ISB energy spacing between individual levels. The same parameters as in Eq. (8) are used in the calculations of Eq. (9). We calculate a global IFR relaxation time for the upper laser level, state 3, of $\sim$0.724 ps.

For $\eta_{inj,tot}$, we obtain a value of 0.94 using calculated values of 0.97 for both η_{inj} and η_p.[11] The relatively high value for η_p is a reflection of both high E_{43} (84.4 meV) and τ_{43} (0.51 ps) values, which lead to negligible leakage current [see Eq. (4)]. Using total values (i.e., including IFR scattering) for τ_{3g}, $\tau_{22'g}$ and τ_{32g}, we obtain a total value for $\tau_{up,g}$ of 0.428 ps. Then, the gain coefficient g is calculated to be 3.14 cm/kA and is kept constant along with the waveguide loss for all simulations following.

Asymmetry of transverse-field profiles (as seen in Fig. 4) is due to the unequal thicknesses of the optical-confinement layers employed in these designs (Fig. 4). These thicknesses are chosen in accordance with the optimization of the Γg product and the sum of losses ($\alpha_{tot} = \alpha_m + \alpha_{w,sim} + \alpha_{isb,bf}$) in order to obtain the lowest J_{th} value. For a fixed lower-cladding thickness of 2 μm and upper-cladding thickness of 3.5 μm, the best-case scenarios with highest Γ, lowest α_{tot}, and lowest J_{th} values are shown in Fig. 4.

On observing that InAlAs is the material of choice over InGaP in order to obtain the lowest J_{th} value for these QCLs (Table 6), the impact of varying the thickness of the lower-cladding layer is studied for 3-mm-long, HR-coated devices. It is evident that the 3-μm-thick InAlAs lower-cladding configuration is theoretically the best in terms of the confinement factor and loss coefficient α_{sim}, and that the J_{th} value is expected to be only $\sim$10% higher than that for the 4.6-μm-emitting QCL. There is room for improvement by increasing the cavity length to 5 mm in order to reduce α_m and consequently, J_{th}. That is, for $L = 5$ mm, the J_{th} value decreases to 0.99 kA/cm^2 for the 3-μm-thick InAlAs lower-cladding design. Additionally, this configuration results in a symmetric mode profile owing to equal lower and upper confinement layer thicknesses, again obtained by minimizing the α_{tot}/Γ quantity.

We also performed a thermal analysis that provides understanding of heat dissipation in 3.4-μm-emitting QCLs on MBL with InAlAs and InGaP cladding layers when compared to an InP-cladding 4.6-μm QCLs.[51] InP is the obvious cladding-layer choice for InP-based QCLs being a well-characterized binary material with high thermal conductivity (68.03 W/m · K).[30,31]


(a)

(b)
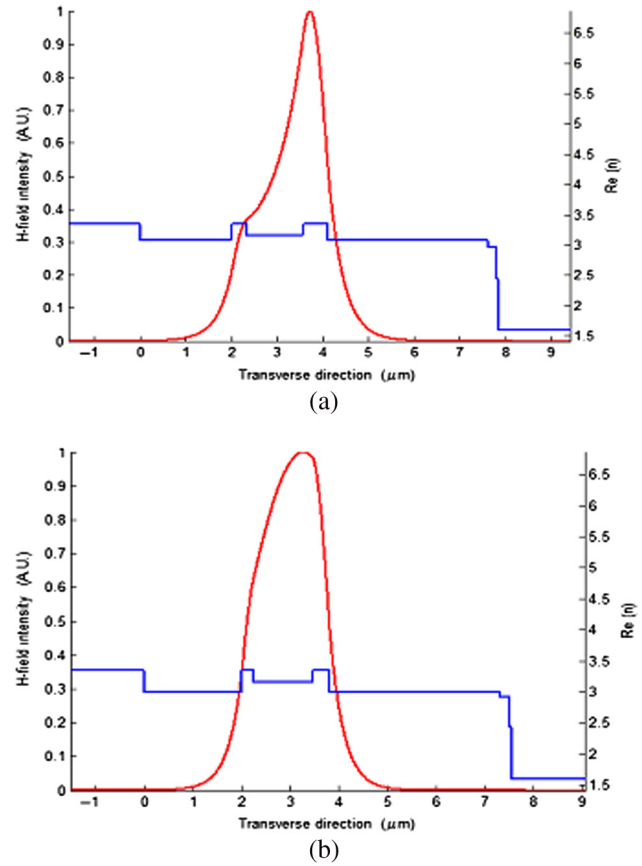
Fig. 4 Simulation of magnetic-field intensity profile of the fundamental transverse mode for the complete laser structure with 2-μm-thick (a) $In_{0.69}Ga_{0.31}P$ (b) $In_{0.21}Al_{0.79}As$ lower-cladding layers.

The thermal dissipation simulation is performed on a model using the best configuration obtained from optical-mode analysis for the 3.4-μm-emitting QCL using InAlAs cladding layers [Fig. 5(c)]. This is compared to QCL structures with InP and InGaP cladding layers as to analyze the effectiveness of these materials as thermally conducting cladding layers [Figs. 5(a) and 5(b)]. 10-μm-wide and 5-mm-long ridge structures are considered, with a Si_3N_4 current-confinement dielectric layer, and plated Au around and above the ridge.

Table 6 Comparison of InGaP versus InAlAs as lower-cladding layers for 3.4-μm-emitting QCLs, and of 3.4-μm-emitting QCLs on MBL versus 4.6-μm-emitting QCL.[45]

Lower cladding material/thickness	4.6-μm QCL on InP[45]	3.4-μm QCL on MBL		
		2-μm InGaP	2-μm InAlAs	3-μm InAlAs
α_{sim} (cm^{-1})	—	2.559	1.786	0.811
Γ	0.67	0.48	0.641	0.691
J_{th} (kA/cm^2)	1.28	3.18	2.00	1.40
Lower confinement (μm)	—	0.35	0.25	0.15
Upper confinement (μm)	—	0.55	0.35	0.15
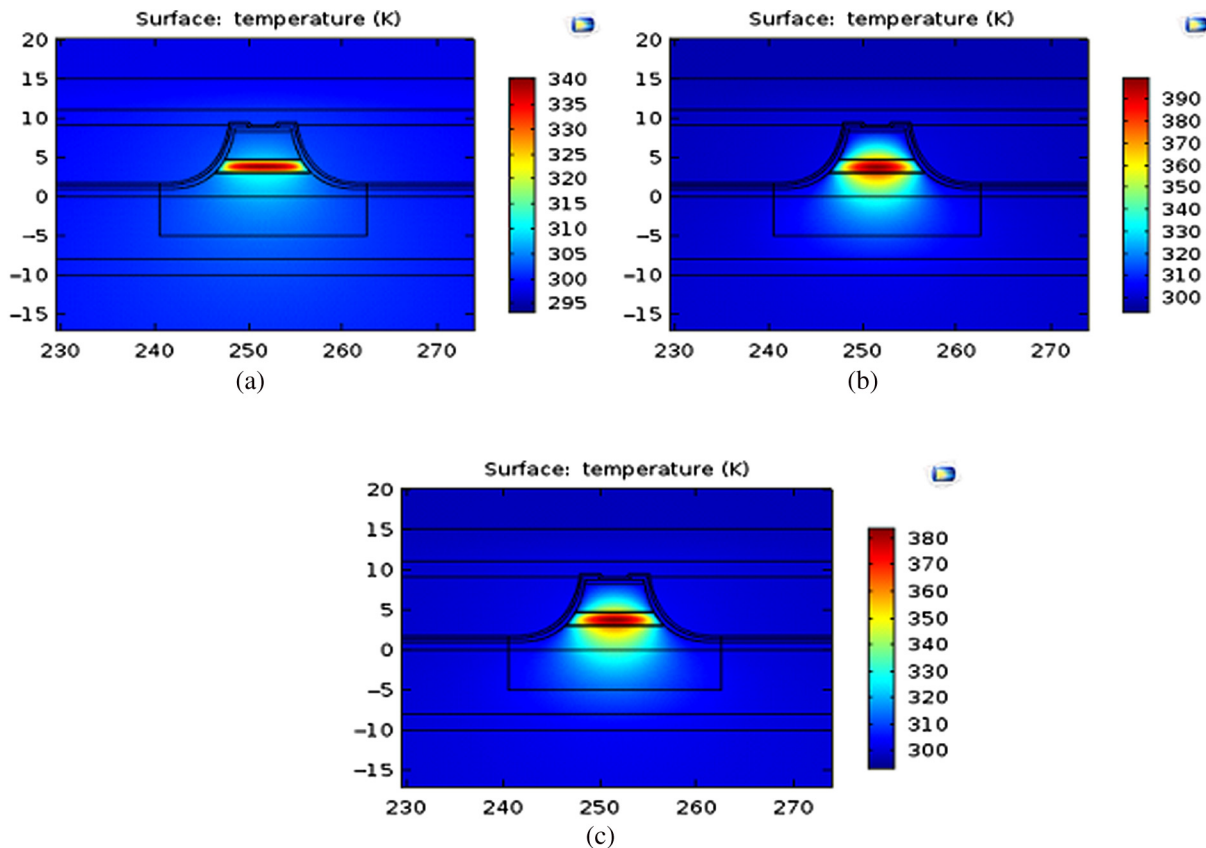
Fig. 5 Simulated thermal dissipation for the complete laser structure in a 5-mm-long device with: (a) InP, (b) $In_{0.69}Ga_{0.31}P$, and (c) $In_{0.21}Al_{0.79}As$ cladding layers.

To quantify this heat dissipation, we look at the average temperature rise, ΔT_{act}, in the core region with respect to the heatsink temperature, which is taken to be room temperature. We assume 5% CW wallplug efficiency for the input power (i.e., 95% of the input power will be dissipated as heat). The 5% value is chosen to be about twice that obtained for 3.56-μm-emitting QCLs[14] at room temperature (i.e., $\sim$2.5%), since our structure has carrier-leakage suppression which has been shown[36] to result in basically doubling of the CW wall-plug efficiency value compared to devices with significant carrier leakage. The ΔT_{act} value for structures with InP, InGaP, and InAlAs claddings, given 15 W of input power, is 33.6, 74.6, and 63.8 K, respectively. That is, using InAlAs claddings increases ΔT_{act} by a factor of $\sim$1.9 compared to when using InP claddings and decreases ΔT_{act} by $\sim$15% to when using InGaP claddings. The former illustrates the expected penalty in thermal conduction for short-wavelength QCLs employing ternary-cladding layers lattice matched to the virtual-substrate layers atop MBLs.

4 Conclusions

A mid-IR QCL with an emission wavelength of 3.4 μm is designed for a virtual substrate of the composition $In_{0.22}Ga_{0.78}As$. This design has the advantage of depopulation of the lower laser level involving both the SPR scheme and resonant-tunneling extraction to the extractor/injector region. In turn, one obtains fast, miniband-like carrier extraction from the AR. Scattering due to IFR is taken into account to estimate an EL linewidth of 54.6 meV for this device. Utilizing both elastic and inelastic lifetimes, the J_{th} value

is projected to be as low as 1.4 kA/cm^2 for 3-mm-long, HR-coated devices. The thermal and optical characteristics of InAlAs-cladding and InGaP-cladding structures for the presented QCL design on MBLs are analyzed. InAlAs is computationally shown to be more effective than InGaP in confining the optical field as well as better for dissipating the generated heat. There is, however, a penalty in the heat dissipation of such a QCL owing to the requirement of a ternary cladding layer lattice matched to the MBL when compared to the InP-based QCLs employing InP claddings. Future work includes verification of the thermal conductivities of the specific compositions of InAlAs and InGaP grown on the MBL, and growth and characterization of QCLs with these cladding layers.

References

1. L. Shterengas et al., "Continuous wave operation of diode lasers at 3.36 μm at 12°C," *Appl. Phys. Lett.* **93**, 011103 (2008).
2. L. Shterengas et al., "Diode lasers emitting at 3 μm with 300 mW of continuous-wave output power," *Electron. Lett.* **45**, 942 (2009).

3. T. Hosoda et al., "Diode lasers emitting near 3.44 μm in continuous-wave regime at 300K," *Electron. Lett.* **46**, 1455 (2010).
4. I. Vurgaftman et al., "Mid-infrared interband cascade lasers operating at ambient temperatures," *New J. Phys.* **11**, 125015 (2009).
5. I. Vurgaftman et al., "Interband cascade lasers with low threshold powers and high output powers," *IEEE J. Sel. Top. Quantum Electron.* **19**, 1200210 (2013).
6. I. Vurgaftman et al., "Interband cascade lasers," *J. Phys. D: Appl. Phys.* **48**, 123001 (2015).
7. W. W. Bewley et al., "Lifetimes and Auger coefficients in type-II W interband cascade lasers," *Appl. Phys. Lett.* **93**, 041118 (2008).
8. D. A. Firsov et al., "Dynamics of photoluminescence and recombination processes in Sb-containing laser nanostructures," *Semiconductors* **44**, 50–58 (2010).
9. D. Botez, "Design considerations and analytical approximations for high continuous-wave power, broad-waveguide diode lasers," *Appl. Phys. Lett.* **74**, 3102–3104 (1999).
10. D. Botez et al., "Electron leakage and its suppression via deep-well structures in 4.5- to 5.0-μm-emitting quantum cascade lasers," *Opt. Eng.* **49**, 111108 (2010).
11. D. Botez, C.-C. Chang, and L. J. Mawst, "Temperature sensitivity of the electro-optical characteristics for mid-infrared ($\lambda = 3$-16 μm)-emitting quantum cascade lasers," *J. Phys. D: Appl. Phys.* **49**(4), 043001 (2016).
12. P. Franzosi and G. Silviati, "Misfit dislocations in InGaAs/InP MBE single heterostructures," *J. Cryst. Growth* **75**, 521–534 (1986).
13. R. Beanland, D. J. Dunstan, and P. J. Goodhew, "Plastic relaxation and relaxed buffer layers for semiconductor epitaxy," *Adv. Phys.* **45**, 87–146 (1996).
14. N. Bandyopadhyay et al., "High power, continuous wave, room temperature operation of $\lambda \sim 3.4$ μm and $\lambda \sim 3.55$ μm InP-based quantum cascade lasers," *Appl. Phys. Lett.* **100**, 212104 (2012).
15. A. Aldukhayel et al., "Investigations of carrier scattering into L-valley in $\lambda = 3.5$ μm InGaAs/AlAs(Sb) quantum cascade lasers using high hydrostatic pressure," *Phys. Status Solidi B* **250**(4), 693–697 (2013).
16. A. Bismuto, M. Beck, and J. Faist, "High power Sb-free quantum cascade laser emitting at 3.3 μm above 350 K," *Appl. Phys. Lett.* **98**, 191104 (2011).
17. N. Bandyopadhyay et al., "Room temperature continuous wave operation of $\lambda \sim 3$-3.2 μm quantum cascade lasers," *Appl. Phys. Lett.* **101**, 241110 (2012).
18. M. P. Semtsiv et al., "Short-wavelength ($\lambda \approx 3.05$ μm) InP based strain-compensated quantum-cascade laser," *Appl. Phys. Lett.* **90**, 051111 (2007).
19. L. J. Mawst et al., "InGaAs/AlInAs strain-compensated superlattices grown on metamorphic buffer layers for low-strain, 3.6 μm-emitting quantum-cascade-laser active regions," *J. Cryst. Growth* **370**, 230–235 (2013).
20. A. Rajeev et al., "Regrowth of quantum cascade laser active regions on metamorphic buffer layers," *J. Cryst. Growth* **452**, 268–271 (2016).
21. L. J. Mawst et al., "Low-strain, quantum-cascade-laser active regions grown on metamorphic buffer layers for emission in the 3.0-4.0 μm wavelength region," *IET Optoelectron.* **8**, 25–32 (2014).
22. B. T. Zutter et al., "Planarization and processing of metamorphic buffer layers grown by hydride vapor phase epitaxy," *J. Electron. Mater.* **43**(4), 873–878 (2014).
23. N. Bandyopadhyay et al., "Watt level performance of quantum cascade lasers in room temperature continuous wave operation at $\lambda \sim 3.76$ μm," *Appl. Phys. Lett.* **97**, 131117 (2010).
24. J. D. Kirch et al., "86% internal differential efficiency from 8-9 μm-emitting, step-taper active-region quantum cascade lasers," *Opt. Express* **24**, 24483–24494 (2016).
25. S. Li et al., "Analysis of surface emitting second-order distributed feedback lasers with central grating phase shift," *IEEE J. Sel. Top. Quantum Electron.* **9**(5), 1153–1165 (2003).
26. M. A. Ordal et al., "Optical properties of Au, Ni, and Pb at submillimeter wavelengths," *Appl. Opt.* **26**(4), 744–752 (1987).
27. M. A. Ordal et al., "Optical properties of Al, Fe, Ti, Ta, W, and Mo at submillimeter wavelengths," *Appl. Opt.* **27**(6), 1203–1209 (1988).
28. R. P. Leavitt et al., "High-performance quantum cascade lasers in the 7.3- to 7.8-μm wavelength band using strained active regions," *Opt. Eng.* **49**, 111109 (2010).
29. S. Adachi, "Lattice thermal resistivity of III–V compound alloys," *J. Appl. Phys.* **54**(4), 1844–1848 (1983).
30. W. Nakwaski, "Thermal conductivity of binary, ternary, and quaternary III-V compounds," *J. Appl. Phys.* **64**(1), 159–166 (1988).
31. H. Yang et al., "Thermal resistance of metamorphic InP-based HBTs on GaAs substrates using a linearly graded In$_x$Ga$_{1-x}$P metamorphic buffer," *IEEE Trans. Electron Devices* **51**(8), 1221–1227 (2004).
32. H. K. Lee and J. S. Yu, "Thermal effects in quantum cascade lasers at $\lambda \sim 4.6$ μm under pulsed and continuous-wave modes," *Appl. Phys. B* **106**(3), 619–627 (2012).
33. M. Razeghi, "High-performance InP-based mid-IR quantum cascade lasers," *IEEE J. Sel. Top. Quantum Electron.* **15**(3), 941–951 (2009).
34. R. Jin, Sub-nanosecond pulse characteristics of InGaP/GaAs HBTs, Lehigh Preserve, Page 7, http://preserve.lehigh.edu/cgi/viewcontent.cgi?article=2333&context=etd.
35. W. Both and F. P. Herrmann, "Thermal resistivity of quaternary solid solution Ga$_x$In$_{1-x}$As$_y$P$_{1-y}$ lattice matched to InP and GaAs," *Cryst. Res. Technol.* **17**, K117 (1982).
36. D. Botez et al., "Multidimensional conduction-band engineering for maximizing the continuous-wave (CW) wallplug efficiencies of mid-infrared quantum cascade lasers," *IEEE J. Sel. Top. Quantum Electron.* **19**(4), 1200312 (2013).
37. J. Faist, *Quantum Cascade Lasers*, pp. 112–114, Oxford University Press, United Kingdom (2013).
38. D. Botez et al., "Temperature dependence of the key electro-optical characteristics for midinfrared emitting quantum cascade lasers [Appl. Phys. Lett. 97,199901 (2010)]," *Appl. Phys. Lett.* **97**, 071101 (2010).
39. D. Botez, "Comment on 'Highly temperature insensitive quantum cascade lasers' [Appl. Phys. Lett. 97, 251104, (2010)]," *Appl. Phys. Lett.* **98**, 216101 (2011).
40. D. Botez et al., "The temperature dependence of key electro-optical characteristics for mid-infrared emitting quantum cascade lasers," *Proc. SPIE* **7953**, 79530N (2011).
41. J. C. Shin et al., "Highly temperature insensitive, deep-well 4.8 μm-emitting quantum cascade semiconductor lasers," *Appl. Phys. Lett.* **94**, 201103 (2009).
42. J. P. Commin et al., "High peak power $\lambda \sim 3.3$ and 3.5 μm InGaAs/AlAs (Sb) quantum cascade lasers operating up to 400 K," *Appl. Phys. Lett.* **97**, 031108 (2010).
43. Y. V. Flores et al., "Thermally activated leakage current in high-performance short-wavelength quantum cascade lasers," *J. Appl. Phys.* **113**, 134506 (2013).
44. R. Maulini et al., "High power thermoelectrically cooled and uncooled quantum cascade lasers with optimized reflectivity facet coatings," *Appl. Phys. Lett.* **95**, 151112 (2009).
45. A. Lyakh et al., "1.6 W high wall plug efficiency, continuous-wave room temperature quantum cascade laser emitting at 4.6 m," *Appl. Phys. Lett.* **92**, 111110 (2008).
46. C. Pflügl et al., "Activation energy study of electron transport in high performance short wavelengths quantum cascade lasers," *Opt. Express* **18**(2), 746–753 (2010).
47. J. B. Khurgin, "Inhomogeneous origin of the interface roughness broadening of intersubband transitions," *Appl. Phys. Lett.* **93**, 091104 (2008).
48. A. Wittmann et al., "Intersubband linewidths in quantum cascade laser designs," *Appl. Phys. Lett.* **93**, 141103 (2008).
49. J. B. Khurgin et al., "Role of interface roughness in the transport and lasing characteristics of quantum-cascade lasers," *Appl. Phys. Lett.* **94**, 091101 (2009).
50. Y. T. Chiu et al., "Importance of interface roughness induced intersubband scattering in mid-infrared quantum cascade lasers," *Appl. Phys. Lett.* **101**, 171117 (2012).
51. Y. Bai et al., "Room temperature continuous wave operation of quantum cascade lasers with watt-level optical power," *Appl. Phys. Lett.* **92**, 101105 (2008).

Ayushi Rajeev received her BTech degree in electronics and communication engineering from Manipal University, India, in 2011 and her MS degree from Columbia University, New York, in 2013. She is currently a PhD candidate with specialization in solid-state electronics and photonics at the University of Wisconsin–Madison. Her research interests include device modeling and MOCVD growth of mid-infrared (IR) quantum cascade lasers (QCLs) on innovative substrates along with the study of group III/V interfacial characteristics.

Chris Sigler received his BS degree in computer engineering from Michigan State University, East Lansing, Michigan, in 2012. He is currently working toward his PhD in the Department of Electrical and Computer Engineering, the University of Wisconsin–Madison. His graduate studies have focused on the simulation and fabrication of QCLs, particularly on high-power QCL arrays and grating-coupled surface-emitting QCLs.

Tom Earles received his BS and MS degrees in electrical engineering. In 1999, he left graduate school to cofound a diode laser manufacturing company, Alfalight Inc. He is currently the director of product development for Intraband LLC, which is developing high-power QCLs.

Yuri V. Flores received his BS degree in physics from the Leibniz University Hannover, Germany, in 2010 and his MS and PhD degrees in physics from the Humboldt University Berlin, Germany, in 2013 and 2015, respectively. In 2016, he joined as postdoctoral research fellow at the Research Laboratory of Electronics, the Massachusetts Institute of Technology. He has authored or coauthored 22 technical papers, and his current research interests include semiconductor mid-IR and terahertz lasers, miniaturized IR sensors, and terahertz time-domain spectroscopy.

Luke J. Mawst received his BS degree in engineering physics and his MS and PhD degrees in electrical engineering from the University of Illinois at Urbana–Champaign in 1982, 1984, and 1987, respectively. He is currently a professor in the Electrical and Computer Engineering Department, the University of Wisconsin–Madison, where he is involved in the development of innovative III/V compound semiconductor device structures, including QCLs, leaky-mode photonic crystal lasers, and high-power diode lasers. He has authored or coauthored more than 250 technical journal articles and holds 26 patents. He is a fellow of IEEE and member of OSA.

Dan Botez has received his BS, MS, and PhD degrees in electrical engineering from the University of California–Berkeley in 1971, 1972, and 1976, respectively. He is currently the Philip Dunham Reed professor of electrical engineering at the University of Wisconsin–Madison. His current research interests lie in three areas of semiconductor-laser device physics: QCLs; high-power, coherent edge-emitting lasers; and high-power, coherent grating-coupled surface-emitting lasers. He has authored or coauthored more than 450 technical publications, of which over 340 were refereed, and holds 56 patents. He is a fellow of the IEEE and the OSA.